Atmospheric Research 274 (2022) 106196

Contents lists available at ScienceDirect

Atmospheric Research

journal homepage: www.elsevier.com/locate/atmosres

Unevenly distributed CO_2 and its impacts on surface energy balance

Wei Cheng [a,b,*], Xiaonan Duan [c], John C. Moore [d,e,f], Xiangzheng Deng [a,b,g,*], Yong Luo [h], Lei Huang [h], Yongli Wang [i]

[a] Institute of Geographic Sciences and Natural Resources Research, Chinese Academy of Sciences, Beijing 100101, China
[b] Key Laboratory of Land Surface Pattern and Simulation, Chinese Academy of Sciences, Beijing 100101, China
[c] Bureau of Frontier Sciences and Education Chinese Academy of Sciences, Beijing 100864, China
[d] College of Global Change and Earth System Science, Beijing Normal University, Beijing 100875, China
[e] CAS Center for Excellence in Tibetan Plateau Earth Sciences, Beijing 100101, China
[f] Arctic Centre, University of Lapland, Rovaniemi 96101, Finland
[g] University of Chinese Academy of Sciences, Beijing 100049, China
[h] Department of Earth System Science, Ministry of Education Key Laboratory for Earth System Modeling, Institute for Global Change Studies, Tsinghua University, Beijing 100084, China
[i] National Institute of Natural Hazards, Ministry of Emergency Management of China, Beijing 100085, China

ARTICLE INFO

Keywords:
Non-uniform CO_2 distribution
BNU-ESM
Surface radiation budget
Net surface longwave radiation
Cloud radiative forcing

ABSTRACT

Atmospheric carbon dioxide (CO_2) has affected global surface and atmospheric energy balance since the Industrial Revolution. The spatial distribution of CO_2 concentrations derived from satellite observation are introduced into the coupled Beijing Normal University Earth System Model (BNU-ESM) to study the responses of temperature and surface energy balance to non-uniform CO_2 distribution under the Representative Concentration Pathway 8.5 scenario to 2100. Global annual mean atmospheric CO_2 concentrations are set to equal those specified in the standard uniform CO_2 simulations with differences in spatial pattern and seasonal cycles amounting to tens of ppm. Relative to the uniform CO_2 simulation, global annual mean surface air temperature increases by 0.44 ± 0.03 °C over 2071–2100 when forced with non-uniformly distributed CO_2, in the Arctic by 1.63 ± 0.28 °C and by 0.67 ± 0.08 °C in northern midlatitudes. The non-uniform CO_2 simulation increases global surface energy by 0.68 ± 0.06 W m^{-2}, principally due to a 0.73 ± 0.08 W m^{-2} increase in net downward surface longwave flux. Surface energy balance increases by 0.33 ± 0.11 W m^{-2} (7.4%) averaged over oceans indicting a significant increase in ocean heat uptake. Surface energy budget averaged over the Arctic summer increases by 0.91 ± 0.68 W m^{-2} in the non-uniform CO_2 simulation, which would have impact on sea ice extent and land ice melt rates with associated feedbacks. The increased surface energy fluxes and temperatures imply reduced time and emission space for greenhouse gases before running into scientific and politically flagged temperature limits.

1. Introduction

Increasing atmospheric greenhouse gas concentrations, in particular CO_2, are the main drivers of global warming, as they trap infrared radiation emitted from the Earth and warm the atmosphere and surface. Both surface and satellite observations have been used to monitor atmospheric CO_2 concentrations. There are about 156 CO_2 measurement stations in 47 countries monitoring atmospheric CO_2 at the surface within the National Oceanic and Atmospheric Administration Earth System Research Laboratory (NOAA ESRL) network. Additionally, about 20 surface stations use a ground-based Fourier transform spectrometer to measure column CO_2 in the Total Carbon Column Observing Network (TCCON) (Wunch et al., 2011). Recent satellite CO_2 retrievals provide continuous global maps of both column CO_2, e.g., from the Orbiting Carbon Observatory 2 (OCO-2) satellite (Kuang et al., 2002), the Greenhouse gases Observing SATellite (GOSAT) (Kuze et al., 2009) and the Chinese Global Carbon Dioxide Monitoring Scientific Experimental Satellite (TanSat) (Yang et al., 2021); and also mid-tropospheric CO_2, e.g., the Atmospheric Infrared Sounder (AIRS) (Chahine et al., 2008). Although some regional discrepancies between the satellite products have been attributed to lack of independent reference observations constraints, the satellite-derived distributions of tropospheric CO_2 are

* Corresponding authors at: Institute of Geographic Sciences and Natural Resources Research, Chinese Academy of Sciences, Beijing 100101, China.
E-mail addresses: chengwei@igsnrr.ac.cn (W. Cheng), dengxz@igsnrr.ac (X. Deng).

https://doi.org/10.1016/j.atmosres.2022.106196
Received 22 November 2021; Received in revised form 24 February 2022; Accepted 10 April 2022
Available online 13 April 2022

generally consistent with each other (Wang et al., 2013; Yang et al., 2021).

The AIRS sensor on the Aqua satellite provides a continuous daily CO_2 retrieval distribution using absorption bands at 690–725 cm^{-1} from 60°S to 90°N, and reveals the nonuniform distribution of mid-tropospheric CO_2 concentrations (Cao et al., 2019). The AIRS-retrieved data has also been validated with in situ measurements (Chahine et al., 2008) and airborne platform observations (Cao et al., 2019) indicating high stability and an accuracy better than 2 ppm (Chahine et al., 2005). Relatively high CO_2 concentrations (30°N-60°N) regions arise from high CO_2 emission ground sources combined with wind advection systems (Fig. A.1; Cao et al., 2019; Ying et al., 2020). The areas with low atmospheric CO_2 concentrations are mainly at high latitudes in the northern hemisphere (NH) and as far south as measurements extend (50°S-60°S). These globally distributed CO_2 retrievals from satellites offer a unique opportunity to explore atmospheric CO_2 variability at the planetary scale. Observed mean spatial CO_2 concentrations seem to vary by about 10 ppm, while seasonally variations can be more than 20 ppm in northern mid latitudes (Fig. A.1; Cao et al., 2019).

Relatively few climate simulation studies have been based on a globally non-uniform mean CO_2 distribution patterns (Navarro et al., 2018; Wang et al., 2020; Xie et al., 2018; Zhang et al., 2019). Those that have been done lead to a 0.2 °C reduction in bias of historical temperature simulation in climate models. Direct radiative forcing from inhomogeneous CO_2 variations of around 10 ppm would only lead to radiative forcing differences of 0.1–0.2 W m^{-2}, apparently far too small to create the temperature differences seen in the simulations. However, Arctic amplification responsible for the Arctic warming two or three times faster than the rest of the planet has been ascribed to locally elevated CO_2 concentrations (Stuecker et al., 2018). This suggests that the response of Earth system to the actual nonuniform CO_2 distribution may be important for large scale temperature, moisture and atmospheric transport variability.

Historical simulations have been done using the Beijing Normal University Earth System Model (BNU-ESM), driven by spatial and seasonally inhomogeneous CO_2 simulations from satellite observation (Wang et al., 2020). While the historical simulation done with the Community Earth System Model (CESM), used spatially inhomogeneous CO_2 prescribed by gridded national-level monthly or annual CO_2 emissions weighted by the grid's population density (Navarro et al., 2018; Zhang et al., 2019). Simulations considering the non-uniform CO_2 mitigate by 0.2 °C global mean overwarming in the standard uniform CO_2 compared with the HadCRUT4 values during 1970–2005 using BUN-ESM (Wang et al., 2020), and smooths the sharp drop of global mean temperature at the end of the period in the uniform simulation using CESM, in agreement with observation (Navarro et al., 2018), indicating that including the heterogenous CO_2 distributions could enhance the realism of global climate modeling, to better anticipate climate system. In addition, Stuecker et al. (2018) found understanding polar amplification primarily requires a better insight into local forcing and feedbacks rather than extra-polar processes, based on climate model simulations in which CO_2 forcing is prescribed in distinct geographical regions, with the sum of climate responses to the regional forcings replicating the response to global forcing.

In this study, we use the BNU-ESM to simulate climate driven by both non-uniform CO_2 concentrations and uniform CO_2 concentrations during the 21st century. All simulations follow the Intergovernmental Panel on Climate Change (IPCC) representative concentration pathway, RCP8.5 CO_2 scenario. By comparing uniform and non-uniform climates from an energetic perspective we illustrate the likely responses of temperature and energy flux to non-uniform CO_2 concentrations during the 21st century. Considering all aspects of the climate system induced by non-uniform CO_2 would be well beyond the scope of any article, but we hope through this perspective to illustrate some of the most important implications.

The rest of the paper is structured as follows. In Section 2 we describe the BNU-ESM, simulation experiments, and surface radiation budget. Section 3.1 describes the results of simulated annual and seasonal changes in temperature as well as land-sea contrast of temperature. Section 3.2 contains analyses of changes in radiative fluxes, i.e., shortwave and longwave radiative fluxes, which induce changes in sensible and latent heat fluxes. Section 3.3 describes changes in cloud radiative forcing, which defined as all-sky minus clear-sky changes in radiative fluxes. Section 3.4 shows analyses of the resulting changes in sensible and latent heat fluxes, which indicate changes in evaporative moisture flux. Section 3.5 includes an evaluation of changes in surface energy balance. In Section 4, we discuss the implications of the differences in climate response to non-uniform CO_2 concentrations in terms of the implied changes in earth system processes. Changes in temperature and surface radiation budget under the non-uniform CO_2 simulation presented in this paper all are compared with the uniform CO_2 simulation.

2. Methods

2.1. Model description

The Beijing Normal University—Earth System Model (BNU-ESM) (Ji et al., 2014) is a fully coupled Earth system model comprising elements representing the atmosphere (NCAR-CAM3.5; Neale et al., 2013), and land surface (BNU-CoLM3; Dai et al., 2003) at a T42 horizontal spectral resolution (approximately 2.81° × 2.81°), ocean (GFDL-MOM4p1; Griffies, 2010) and sea-ice (LANL-CICE4.1; Hunke and Lipscomb, 2010) at a nominal latitude-longitude resolution of 1° (down to 1/3° within 10° of the equatorial tropics) with 360 longitudinal grids and 200 latitudinal grids; and a coupler (improved NCAR-CPL6). It has an interactive carbon cycle model in the land component (BNU-DGVM (C/N)) and an ecosystem-biogeochemical module in the ocean component (IBGC).

Ji et al. (2014) validated the BNU-ESM's performance in terms of the mean model state and the internal variability by comparisons between CMIP5 *piControl* and *historical* simulations and the observed datasets. The 2100 warming in RCP8.5 simulated by BNU-ESM is between the 5th and 95th percentiles range of Earth system models (Sanderson, 2020). The BNU-ESM can in general, simulate observed features of the earth climate system as well as any other Earth System Model, including the climatological annual cycle of surface-air temperature and precipitation, annual cycle of cloud fraction and forcing, terrestrial gross primary productions (GPP) and soil organic carbon stocks. BNU-ESM has proven to be a useful modeling tool and is being actively used by many researchers in prognostic simulations for anthropogenic forcing (e.g., Bracegirdle et al., 2013; Chen et al., 2013; Tian et al., 2016; Wei et al., 2012), solar geoengineered (e.g., Kravitz et al., 2013a, 2013b), and land surface engineered (Cheng et al., 2017) scenarios.

2.2. Simulation experiments

All simulations are forced by the IPCC high-end CO_2 concentration scenario, RCP8.5 (Meinshausen et al., 2011). We carried out two different simulations using BNU-ESM from the year 2005 to 2100, driven by uniform CO_2 and non-uniform CO_2 concentrations separately. In the uniform CO_2 simulation, every grid cell was fixed at the global annual mean CO_2 concentrations under RCP8.5. Temporal and spatial distributions of nonuniform CO_2 under RCP8.5 were generated from satellite observed CO_2 spatial and monthly cycles. Under RCP8.5, the mean non-uniform CO_2 concentrations seem to vary by about 20 ppm, while variations in DJF can be over 30 ppm in northern mid-high latitudes (Fig. 1). The global annual mean of the nonuniform CO_2 concentrations were made consistent with those of the uniform CO_2 concentration simulation (Cheng et al., 2021; Wang et al., 2020; Cheng et al., 2022b). The spinup runs used the derived historical uniform or non-uniform distributions of the CO_2 concentrations from 1850 (Wang

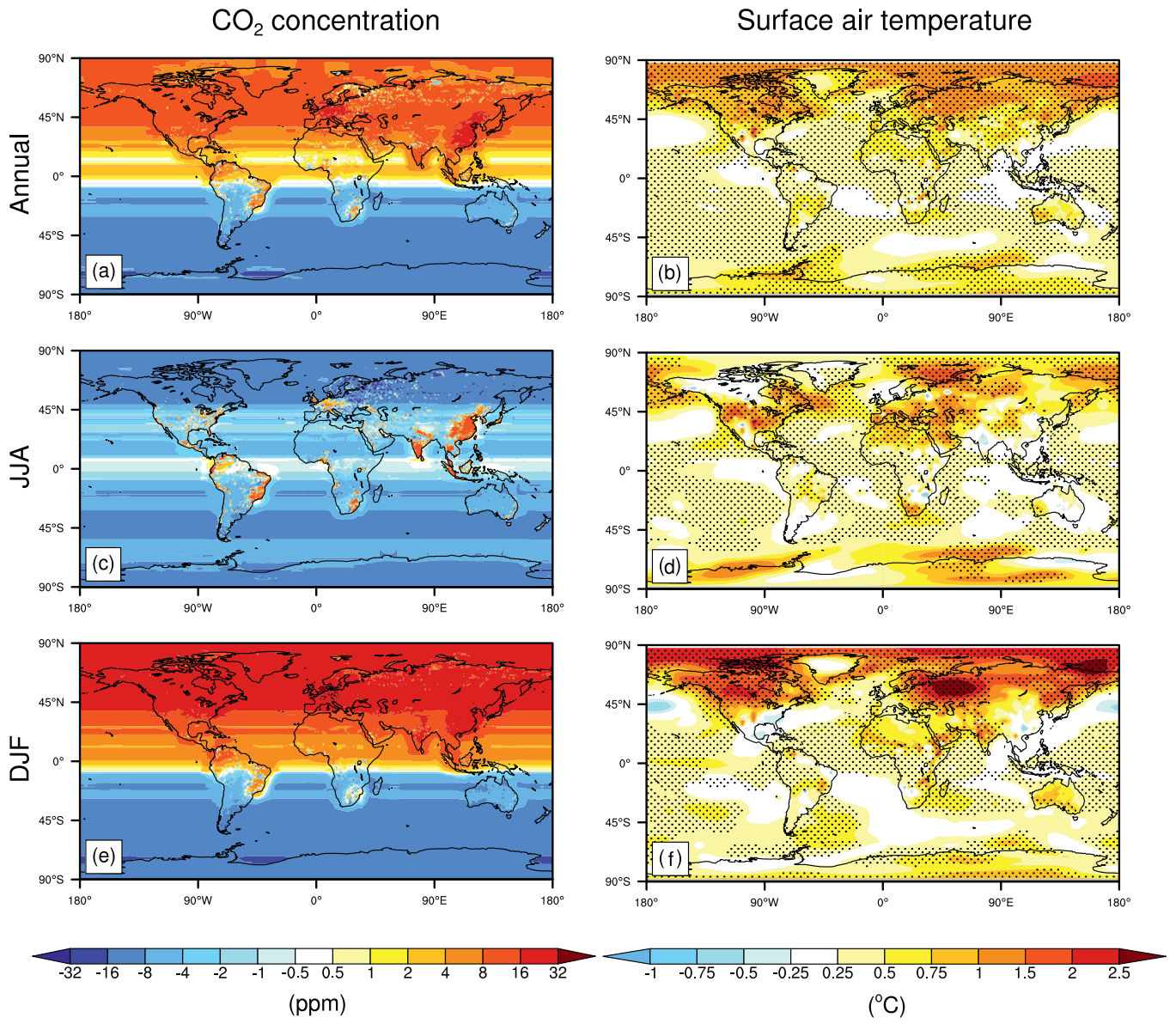

Fig. 1. Maps showing simulated annual mean (a and b), JJA average (c and d), and DJF average (e and f) changes in atmospheric CO_2 concentrations (ppm, left column), and surface air temperature (°C, right column) under non-uniform CO_2 simulation relative to uniform CO_2 simulation during 2071–2100, respectively. Stippling areas in b, d and f are regions where changes are statistically significant at the 5% level using the Student's *t*-test.

et al., 2020). In the non-uniform CO_2 simulation, we consider only radiative forcing from non-uniform CO_2 distribution while other greenhouse gases and aerosols are as in the standard uniform CO_2 simulation.

2.3. Surface radiation budget

The radiation budget at the top of the atmosphere is comprised of shortwave and longwave components. At the surface, any changes in radiative fluxes are compensated by changes in surface turbulent heat fluxes, i.e., sensible and latent heat fluxes (Boer, 1993). More specifically,

$$\rho h c_p \frac{dT}{dt} = SW + LW + SH + LH \quad (1)$$

where ρ denotes the density of the medium (kg m^{-3}), h denotes a length scale associated with ocean heat uptake (m), c_p denotes the specific heat of the surface (W m^{-2} K^{-1}), T is temperature (°C), t is time (s), SW is net solar flux at surface (W m^{-2}), LW is Net longwave flux at surface (W m^{-2}), SH is surface sensible heat flux (W m^{-2}), and LH Surface latent heat flux (W m^{-2}). These abbreviations are consistent throughout the remainder of this paper.

2.4. Statistical analyses

In subsequent analyses we use the average of the RCP8.5 simulation driven by uniform CO_2 concentrations over 2071–2100 as the baseline for comparisons with non-uniform CO_2 concentrations over this period. Differences are quoted with a range indicating the standard error in the difference.

The model outputs are quite Normally distributed and we use Student's *t*-test at each grid point on the maps in the figures. Stippling indicates regions where changes are statistically significant at the 5% level. The Null hypotheses are "non-uniform CO_2 run = uniform CO_2 run" over the period of 2071 to 2100 (n = 30). There are 8192 grid points of annual or seasonal mean BNU-ESM data. The returned

probability for each grid is two-tailed.

Changes under the non-uniform CO_2 simulation in radiative fluxes are calculated over different regions of the globe. The Arctic is defined as all grid boxes North of 66.55°N. The Antarctic is all grid boxes South of 66.55°S. The tropics are all grid boxes between 23.44°S and 23.44°N. The northern and southern midlatitudes are the whole regions between the tropics and the poles.

3. Results

3.1. CO_2 concentration and temperature changes

Both non-uniform and uniform CO_2 simulations have the same mean global atmospheric CO_2 concentrations in each year (Fig. 2a). Annual mean CO_2 concentrations averaged over land increased by 4.11 ± 0.68

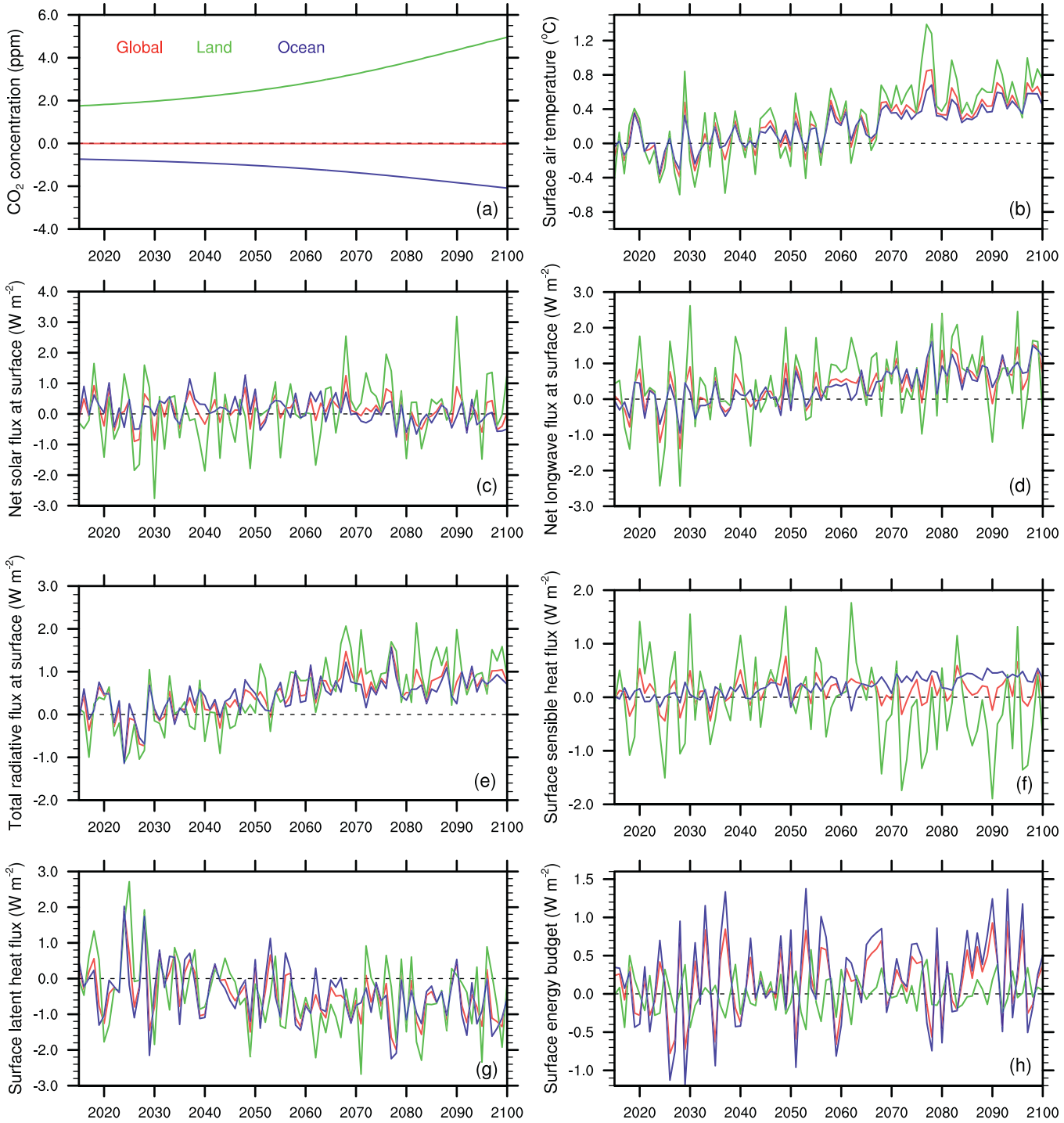

Fig. 2. Global (red), land (green) and ocean (blue) averaged annual time evolution changes in atmospheric CO_2 concentrations (ppm, a), surface air temperature (°C, b), net solar flux at surface (W m^{-2}, c), net longwave flux at surface (W m^{-2}, d), total radiative flux at surface (W m^{-2}, net surface solar flux plus net surface longwave flux, e), surface sensible heat flux (W m^{-2}, f), surface latent heat flux (W m^{-2}, g) and surface energy budget (W m^{-2}, h) under non-uniform CO_2 simulation relative to uniform CO_2 simulation during 2071–2100. Surface energy budget is sum of shortwave radiative fluxes, longwave radiative fluxes, sensible heat fluxes, and latent heat fluxes (the right side of Eq. (1)). All fluxes in c-h are positive in the downward direction. (For interpretation of the references to colour in this figure legend, the reader is referred to the web version of this article.)

ppm in the non-uniform CO_2 simulation over 2071–2100, while CO_2 concentrations decrease by 1.73 ± 0.68 ppm over ocean (Fig. 2a; Table 1), relative to the uniform CO_2 simulation. Which is consistent with features of the current observed distribution of CO_2 concentrations (Cao et al., 2019). In June, July and August (JJA), CO_2 concentrations averaged over land and over ocean decrease by 4.98 ± 0.68 ppm and 5.88 ± 0.68 ppm respectively in the non-uniform CO_2 simulation (Table A.1), related to terrestrial and marine CO_2 absorption in the NH summer (Schimel et al., 2000). In December, January, February (DJF), CO_2 concentrations increase by 9.29 ± 0.71 ppm over land under the non-uniform CO_2 simulation relative to uniform CO_2 simulation (Table A.2). The maximum increase appears in December (11.8 ppm over land), (Fig. A.2a).

Fig. 1 (left column) shows regional differences of atmospheric CO_2 concentrations. Annual and DJF atmospheric CO_2 concentrations in NH are both greater than that in the uniform CO_2 simulation (Figs. 1a, e, A.3a). In DJF, CO_2 concentrations are about 18 ppm higher in the northern midlatitudes and Arctic. At the same time CO_2 concentrations are about 10–12 ppm lower in the southern midlatitudes and the Antarctic. which are mainly due to plant respiration and photosynthesis, and their distribution (Erickson III et al., 2008). In JJA, CO_2 concentrations in the non-uniform CO_2 simulation are mainly lower than those in the uniform CO_2 simulation, except in some high emissions regions such as the eastern United States, South America, western Europe, India, East China, and Southeast Asia (Fig. 1c). Reductions in JJA mean CO_2 concentrations are over 8 ppm in the southern midlatitudes, the Antarctic, and the Arctic in the non-uniform CO_2 simulation. In the tropics, CO_2 concentrations are about 2 ppm higher during DJF and 3 ppm lower during JJA than in the uniform CO_2 runs.

In the non-uniform CO_2 simulation, global annual mean of surface air temperature is 0.44 ± 0.03 °C warmer than that in the uniform CO_2 simulation during 2071–2100 (Fig. 2b; Table 1). Over land temperatures increase by 0.60 ± 0.06 °C and over ocean by 0.37 ± 0.02 °C (Fig. 2b; Table 1), due their differences in heat capacity. Increases in JJA are lower (0.52 ± 0.07 °C for land) than in DJF (0.75 ± 0.10 °C), (Tables A.1, A.2). The maximum monthly mean changes in temperature appear in February with 0.95 °C, and 0.58 °C warming averaged over land and globe during 2071–2100, and the maximum monthly increase over ocean occurs in January and March, each with 0.41 °C warming (Fig. A.2b).

Most of the earth's surface presents statistically significant increases in annual mean surface air temperature under non-uniform CO_2 simulations (Fig. 1b), especially in the mid-to-high latitudes of NH. Relative to the uniform CO_2 simulation, there is 1.07 ± 0.14 °C and 0.58 ± 0.05 °C warming in the Arctic and the northern midlatitudes, respectively, and the warming in the Antarctic is 0.51 ± 0.11 °C under the non-uniform CO_2 simulation. The warming in the Antarctic is caused by longwave cloud forcing (see Section 3.3) and its feedback processes (e.g., sea ice of the Southern Ocean), but not local CO_2 forcing. In JJA, surface air temperature in the non-uniform CO_2 simulation increases by about 0.6 °C in the Arctic, northern midlatitudes and Antarctic relative to the uniform CO_2 simulation. In some regions of the eastern and northwestern United States, and the Barents Sea, the summer warming is more than 1.5 °C in the non-uniform CO_2 simulation (Fig. 1d). In DJF, there is about 0.4 °C warming in the tropics, southern midlatitudes and Antarctic. In the Arctic and northern midlatitudes, warming is about 1.63 ± 0.28 °C and 0.67 ± 0.08 °C, respectively. In some areas of Canada, Russia and Arctic Ocean, the winter warming is over 2.5 °C in the non-uniform CO_2 simulation (Fig. 1f).

3.2. Surface radiative fluxes

Change in CO_2 distribution primarily affects longwave radiation in the free troposphere. Relative to the uniform CO_2 simulation, global annual mean changes in net longwave flux at surface and total radiative flux at surface (net surface solar flux plus net surface longwave flux) increase by 0.73 ± 0.08 W m^{-2} and 0.68 ± 0.06 W m^{-2}, respectively, in the non-uniform CO_2 simulation over 2071–2100 (Figs. 2c, d, e, A.4; Table 1; hereafter all radiative fluxes are positive in the downward direction). The trapping of surface net longwave flux is not only due to increases in annual mean CO_2 concentrations in the NH, but also associated cloud effects (Lengler et al., 2010), that impact short wave solar radiation at the surface. Over land, annual mean net solar and longwave surface fluxes increase by 0.53 ± 0.16 W m^{-2} and 0.51 ± 0.15 W m^{-2}, respectively, in the non-uniform CO_2 simulation, leading to 1.03 ± 0.10 W m^{-2} enhancement of total radiative flux at surface (Fig. 2c, d, e; Table 1). Over ocean, annual mean net longwave flux at surface increases by 0.83 ± 0.06 W m^{-2}, and total radiative flux at surface increases by 0.53 ± 0.06 W m^{-2} in the non-uniform CO_2 simulation due to a 0.30 ± 0.08 W m^{-2} reduction in net surface solar flux (Fig. 2c, d, e; Table 1). In JJA, total radiative fluxes at the surface averaged over land and over ocean increase by 0.52 ± 0.23 W m^{-2} and 0.27 ± 0.13 W m^{-2} respectively in the non-uniform CO_2 simulation, and in DJF total fluxes increase by 1.20 ± 0.16 W m^{-2} over land and 0.59 ± 0.12 W m^{-2} over

Table 1
Annual mean changes globally, averaged over land, averaged over ocean in nonuniform simulation relative to uniform simulation during 2071–2100. Surface energy budget is sum of shortwave radiative fluxes, longwave radiative fluxes, sensible heat fluxes, and latent heat fluxes (the right side of Eq. (1)). Radiative fluxes are positive in the downward direction. Percent changes represent experiment minus the baseline divided by the baseline value. ±range that indicates the standard error in estimating the change.

Annual mean change in nonuniform simulation relative to uniform simulation	Global		Land		Ocean	
	Change	Percentage	Change	Percentage	Change	Percentage
CO_2 (ppm)	−0.02 ± 0.68	−0.00% ± 0.07%	4.11 ± 0.68	0.44% ± 0.07%	−1.73 ± 0.68	−0.18% ± 0.07%
Surface air temperature (°C)	0.44 ± 0.03	2.41% ± 0.18%	0.60 ± 0.06	4.26% ± 0.44%	0.37 ± 0.02	1.86% ± 0.11%
Net solar flux at surface (W m^{-2})	−0.05 ± 0.08	−0.03% ± 0.05%	0.53 ± 0.16	0.36% ± 0.11%	−0.30 ± 0.08	−0.17% ± 0.04%
Net longwave flux at surface (W m^{-2})	0.73 ± 0.08	1.42% ± 0.15%	0.51 ± 0.15	0.87% ± 0.26%	0.83 ± 0.06	1.70% ± 0.13%
Total (shortwave plus longwave) radiative flux at surface (W m^{-2})	0.68 ± 0.06	0.60% ± 0.05%	1.03 ± 0.10	1.16% ± 0.11%	0.53 ± 0.06	0.43% ± 0.05%
Shortwave cloud forcing (W m^{-2})	−0.25 ± 0.07	−0.50% ± 0.14%	−0.10 ± 0.14	−0.23% ± 0.34%	−0.32 ± 0.07	−0.58% ± 0.13%
Longwave cloud forcing (W m^{-2})	−0.06 ± 0.03	−0.25% ± 0.11%	0.08 ± 0.07	0.35% ± 0.31%	−0.12 ± 0.05	−0.47% ± 0.19%
Total (shortwave plus longwave) cloud forcing (W m^{-2})	−0.31 ± 0.07	−1.19% ± 0.26%	−0.02 ± 0.11	−0.10% ± 0.56%	−0.44 ± 0.07	−1.50% ± 0.25%
Surface sensible heat flux (W m^{-2})	0.07 ± 0.04	0.37% ± 0.20%	−0.50 ± 0.13	−1.37% ± 0.36%	0.32 ± 0.02	2.40% ± 0.15%
Surface latent heat flux (W m^{-2})	−0.51 ± 0.11	−0.57% ± 0.12%	−0.48 ± 0.15	−0.93% ± 0.29%	−0.52 ± 0.12	−0.49% ± 0.12%
Surface energy budget (W $m^{-2)}$	0.25 ± 0.08	7.54% ± 2.41%	0.05 ± 0.04	9.60% ± 7.43%	0.33 ± 0.11	7.44% ± 2.60%

ocean (Tables A.1, A.2). A maximum land monthly mean increase in surface total radiative flux of 1.8 W m^{-2} occurs in April during 2071–2100, mainly due to a 2.0 W m^{-2} increase in surface net solar flux over land (Fig. A.2c, e). The maximum rise of 1.0 W m^{-2} in surface total radiative flux over the whole globe and ocean both appear in November, mainly driven by net longwave flux at the surface (Fig. A. 2c, d, e).

Figs. 3 and A.5 show maps of annual mean, JJA average, and DJF average changes in net solar flux, net longwave and total radiative fluxes at the surface relative to uniform CO_2 simulation during 2071–2100. Increases of 1.46 ± 0.39 W m^{-2}, 0.99 ± 0.11 W m^{-2}, 0.35 ± 0.12 W m^{-2} and 0.76 ± 0.10 W m^{-2} in annual mean total radiative flux at surface in the Arctic, northern midlatitudes, tropics and southern midlatitudes, respectively are due to changes in both net solar and net longwave fluxes at surface (Fig. 4). In the non-uniform CO_2 simulation, net shortwave radiative flux decreases by 0.66 ± 0.18 W m^{-2} over the tropics, while net longwave radiative flux increases by 1.01 ± 0.10 W m^{-2}. The increase in longwave flux is associated with increased tropospheric water vapor due to decreased absorption of shortwave radiation by the atmosphere (Kravitz et al., 2013b). The 0.44 ± 0.14 W m^{-2} increase in the Antarctic is decided by change in longwave cloud forcing (Fig. 4). Statistically significant increases in annual mean total radiative flux are primarily located in some areas of the Arctic Ocean, North Greenland, eastern North America, central Asia, Russia, the eastern Pacific and North Atlantic (Fig. A.5). In JJA, surface total radiative flux in the non-uniform CO_2 simulation increases by 0.31 ± 0.27 W m^{-2}, 0.28 ± 0.21 W m^{-2} and 0.45 ± 0.10 W m^{-2} in the northern midlatitudes, tropics and southern midlatitudes, respectively, relative to the uniform CO_2 simulation. Corresponding values in DJF are 0.45 ± 0.17 W m^{-2}, 1.01 ± 0.23 W m^{-2} and 0.61 ± 0.26 W m^{-2}, showing larger values in NH winter. In the Arctic and northern midlatitudes, increases in total

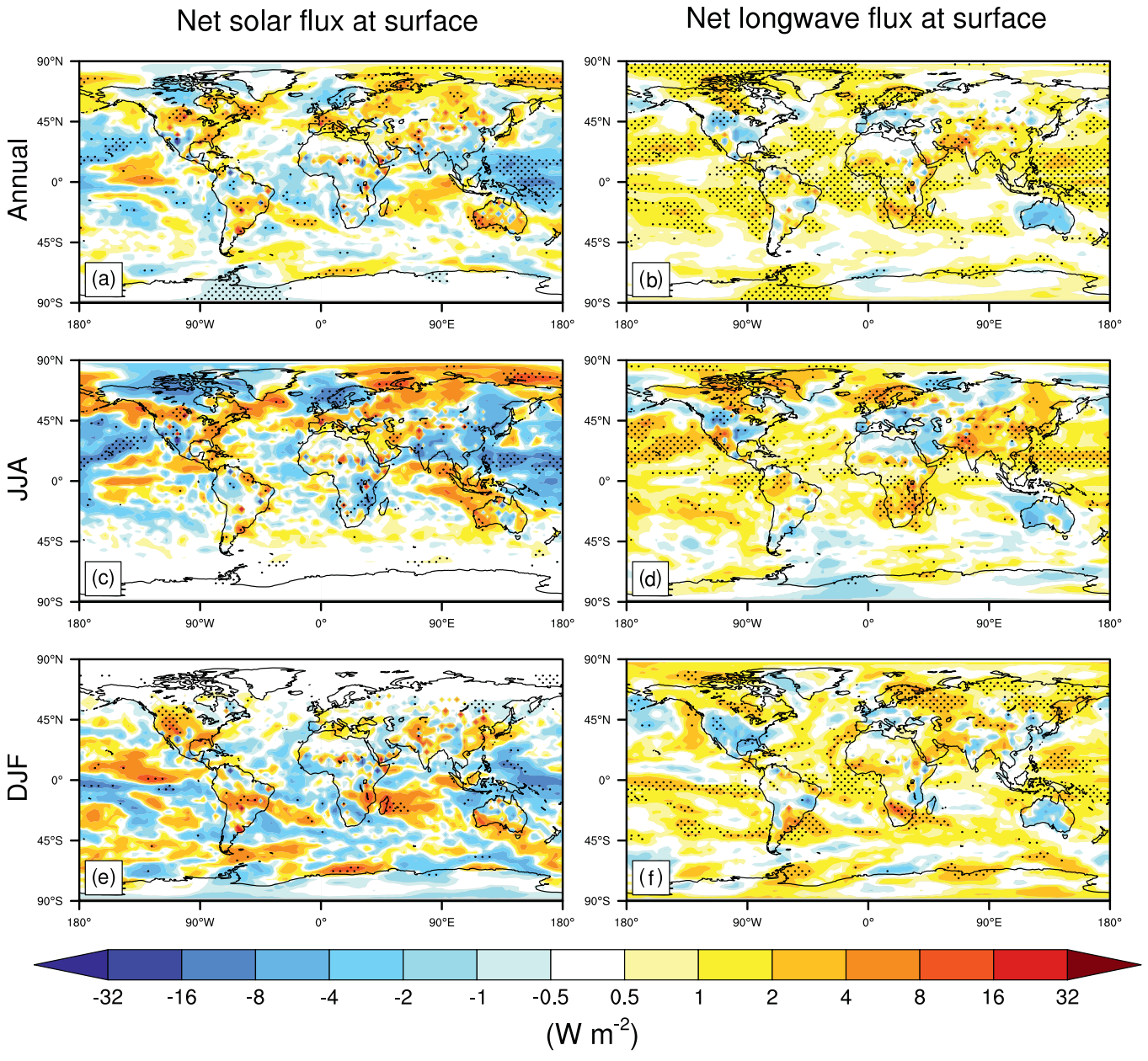

Fig. 3. Maps showing simulated annual mean (a and b), JJA average (c and d), and DJF average (e and f) changes in net solar flux at surface (W m^{-2}, left column) and net longwave flux at surface (W m^{-2}, right column) under non-uniform CO_2 simulation relative to uniform CO_2 simulation during 2071–2100, respectively. Positive values are indicating increases in the downward direction. Stippling areas are regions where changes are statistically significant at the 5% level using the Student's *t*-test.

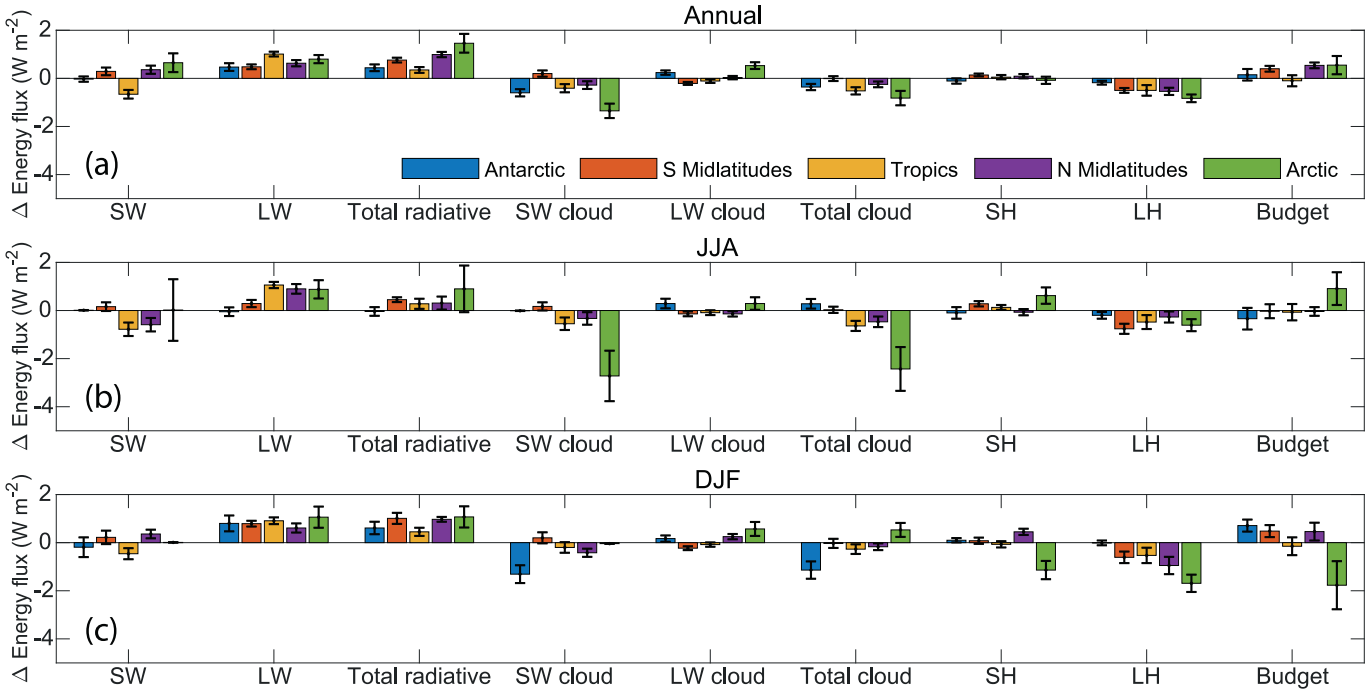

Fig. 4. Bar chart showing annual mean (a), JJA average (b), and DJF average (c) changes in net solar flux at surface (W m^{-2}), net longwave flux at surface (W m^{-2}), total radiative flux at surface (W m^{-2}, net surface solar flux plus net surface longwave flux), shortwave cloud forcing (W m^{-2}), longwave cloud forcing (W m^{-2}), total cloud forcing (W m^{-2}, shortwave cloud forcing plus longwave cloud forcing), surface sensible heat flux (W m^{-2}), surface latent heat flux (W m^{-2}) and surface energy budget (W m^{-2}) under non-uniform CO_2 simulation relative to uniform CO_2 simulation during 2071–2100, averaged over Arctic (green), Antarctic (blue), tropics (yellow), northern midlatitudes (purple) and southern midlatitudes (orange), respectively. Error bars represent standard error. Positive values are indicating increases in the downward direction. Cloud forcing is defined as all-sky minus clear-sky radiative fluxes. Surface energy budget is sum of shortwave radiative fluxes, longwave radiative fluxes, sensible heat fluxes, and latent heat fluxes (the right side of Eq. (1)). The Arctic is defined as all grid boxes North of 66.55°N. The Antarctic is all grid boxes South of 66.55°S. The tropics are all grid boxes between 23.44°S and 23.44°N. The northern and southern midlatitudes are all regions between the tropics and the poles. (For interpretation of the references to colour in this figure legend, the reader is referred to the web version of this article.)

radiative flux are about 1.07 ± 0.44 W m^{-2} and 0.97 ± 0.10 W m^{-2}, respectively (Figs. 4, A.5).

3.3. Cloud radiative forcing

Cloud radiative forcing is defined as all-sky minus clear-sky changes in radiative fluxes, which is mainly caused by changes in cloud fraction (Kravitz et al., 2013b). Relative to the uniform CO_2 simulation, annual mean total cloud forcing (shortwave cloud forcing plus longwave cloud forcing) decreases by 0.31 ± 0.07 W m^{-2} globally and over ocean by 0.44 ± 0.07 W m^{-2} in the non-uniform CO_2 simulation during 2071–2100 (Fig. A.6; Table 1). In JJA, total cloud forcing averaged globally decreases by 0.45 ± 0.12 W m^{-2} and over ocean by 0.55 ± 0.11 W m^{-2}, (Table A.1). In DJF, globally averaged total cloud forcing decreases by 0.18 ± 0.09 W m^{-2} and by 0.27 ± 0.13 W m^{-2} over oceans (Table A.2). The annual, JJA and DJF mean changes in total cloud forcing in the non-uniform CO_2 simulation are mainly determined by changes in shortwave cloud forcing (Fig. A.6; Tables 1, A.1, A.2). The maximum decreases in monthly mean total cloud forcing appear in June with 0.65 W m^{-2} and 0.83 W m^{-2} reductions averaged globally and over ocean, respectively, under non-uniform CO_2 simulation during 2071–2100, and the maximum negative monthly mean change over land occurs in March with 0.75 W m^{-2} reduction, all of which are mainly driven by monthly changes in shortwave cloud forcing (Fig. A.6).

Figs. 5 and A.5 shows maps of annual mean, JJA average, and DJF average changes in shortwave cloud forcing, longwave cloud forcing and total cloud forcing under non-uniform CO_2 simulation relative to uniform CO_2 simulation during 2071–2100. Relative to the uniform CO_2 simulation, there are 0.82 ± 0.30 W m^{-2}, 0.25 ± 0.12 W m^{-2}, 0.52 ± 0.15 W m^{-2} and 0.36 ± 0.13 W m^{-2} decreases in annual mean total cloud forcing in the Arctic, northern midlatitudes, tropics and Antarctic, respectively, in the non-uniform CO_2 simulation (Fig. 4). In the Arctic and Antarctic, decreases in shortwave cloud forcing are partially offset by increases in longwave cloud forcing. In the tropics, the reduction in total cloud forcing is given by 0.41 ± 0.17 W m^{-2} reduction in shortwave cloud forcing and 0.11 ± 0.08 W m^{-2} reduction in longwave cloud forcing. Statistically significant decreases in annual mean total cloud forcing are primarily located in some areas of the Arctic Ocean, northern Canada, western Pacific, and Southern Ocean, while significant increases appear in the southeastern United States and central South America, which are dominated by changes in shortwave cloud forcing (Fig. A.5). In JJA, total cloud forcing in the non-uniform CO_2 simulation decreases by 2.43 ± 0.91 W m^{-2}, 0.47 ± 0.22 W m^{-2} and 0.64 ± 0.21 W m^{-2} in the Arctic, northern midlatitudes and tropics, respectively, relative to the uniform CO_2 simulation, which all are controlled by reductions in shortwave cloud forcing. But in the Antarctic, total cloud forcing increases by 0.28 ± 0.20 W m^{-2} in the non-uniform CO_2 simulation which is mainly from increases in longwave cloud forcing (Figs. 5, A.5). In DJF, there are about 1.14 ± 0.36 W m^{-2}, 0.27 ± 0.20 W m^{-2} and 0.17 ± 0.14 W m^{-2} reductions in total cloud forcing in the Antarctic, tropics and northern midlatitudes in the non-uniform CO_2 simulation compared with the uniform CO_2 simulation, predominantly due to the cloud shortwave effect. In the Arctic, increase in total cloud forcing is about 0.53 ± 0.29 W m^{-2} due to a 0.57 ± 0.29 W m^{-2} increase in longwave cloud forcing in the non-uniform CO_2 simulation (Figs. 4, 5, A.5).

3.4. Sensible and latent heat fluxes

The turbulent heat fluxes, i.e., sensible, and latent heat fluxes, are

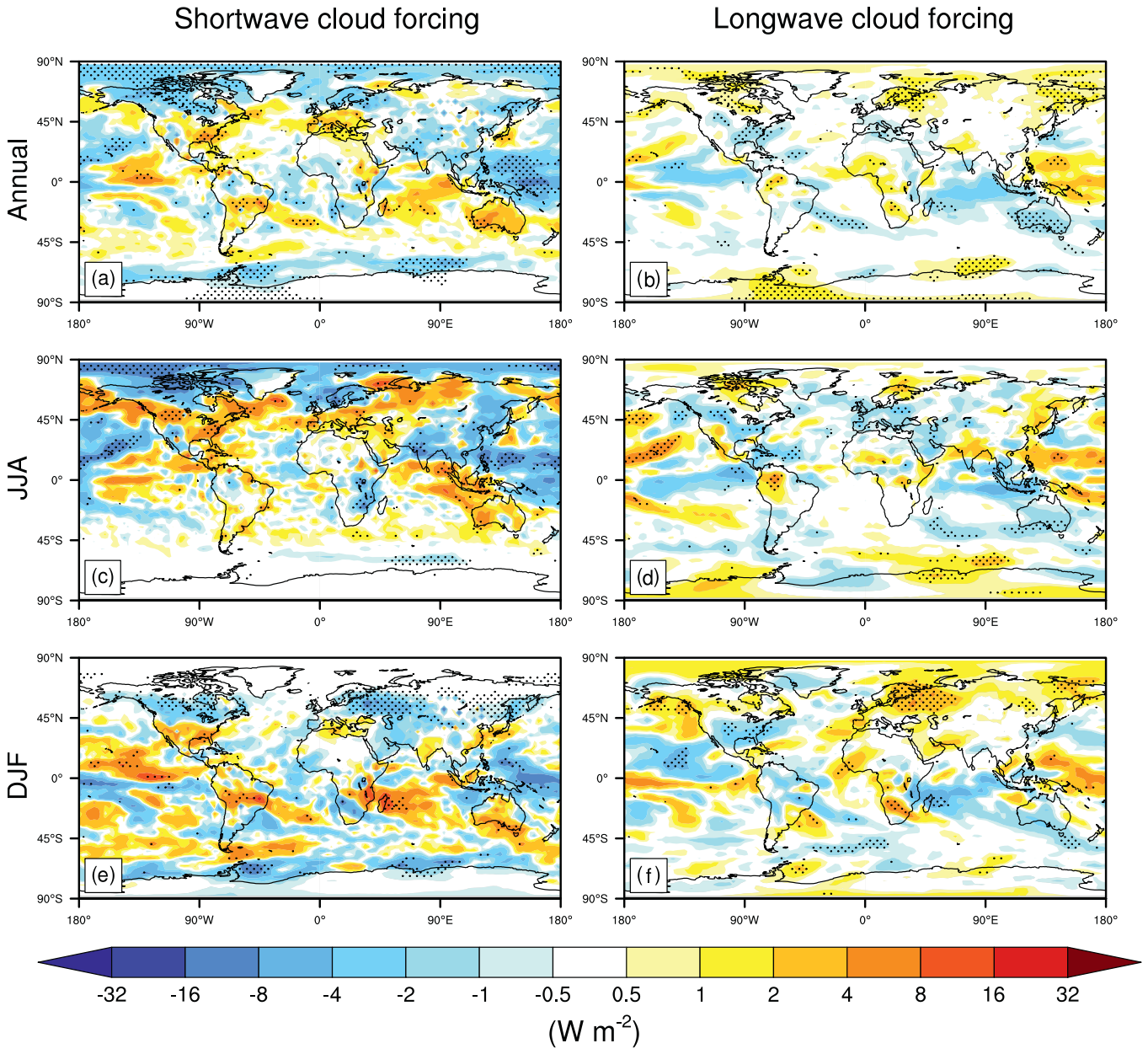

Fig. 5. Maps showing simulated annual mean (a and b), JJA average (c and d), and DJF average (e and f) changes in shortwave cloud forcing (W m^{-2}, left column) and longwave cloud forcing (W m^{-2}, right column) under non-uniform CO_2 simulation relative to uniform CO_2 simulation during 2071–2100, respectively. Positive values are indicating increases in the downward direction. Stippling areas are regions where changes are statistically significant at the 5% level using the Student's *t*-test.

induced by shortwave and longwave radiative fluxes. If change in radiative forcing is not the same at both the surface and the top of the atmosphere, there will be an induced change in the turbulent components at the surface to maintain the tropospheric heat balance (Andrews et al., 2009). The Bowen ratio is defined as the ratio of sensible to latent heat fluxes, i.e.,

$$B = SH/LH \tag{2}$$

A decrease in the Bowen ratio indicates that more energy is used to change the phase of water, implying that region is becoming wetter. Conversely, an increase in the Bowen ratio implies that a region is becoming dryer. This explanation ignores changes in circulation that may result in changes in moisture advection, but it suffices for a global average and explains a significant portion of regional response (Gu et al., 2006). Understanding the climate response to changes in these turbulent fluxes in the non-uniform CO_2 simulation is crucial. Ban-Weiss et al. (2011) showed the balance between surface sensible and latent heating results in cloud feedbacks that alter both global and local temperatures. Note that here positive values indicate a net flux downward, which is the opposite of how turbulent heat fluxes are usually reported.

Relative to the uniform CO_2 simulation, annual mean surface sensible heat flux 2071–2100 increases by 0.07 ± 0.04 W m^{-2} globall, by 0.32 ± 0.02 W m^{-2} over ocean and decreases by 0.50 ± 0.13 W m^{-2} over land (Fig. 2f; Table 1). In JJA, there is a 0.24 ± 0.16 W m^{-2} reduction and 0.28 ± 0.04 W m^{-2} increase in surface sensible heat flux averaged over land and over ocean, respectively (Table A.1). In DJF, surface sensible heat flux decreases by 0.50 ± 0.19 W m^{-2} over land, while it increases by 0.32 ± 0.04 W m^{-2} over ocean (Table A.2). The reduction in surface sensible heat flux averaged over land is associated with warming in the non-uniform CO_2 simulation (Fig. 2f; Tables 1, A.1,

A.2). Land sensible heat flux is lower in all months relative to uniform CO2 simulations with April being most reduced by 0.98 W m^{-2} under non-uniform CO_2 simulation during 2071–2100 (Fig. A.2f).

Fig. 6 (left column) shows maps of annual mean, JJA average, and DJF average changes in surface sensible heat flux under the non-uniform CO_2 simulation relative to the uniform CO_2 simulation during 2071–2100. Statistically significant decreases in annual mean surface sensible heat flux are primarily located in some areas of the Arctic Ocean, southern Canada, eastern United States, Brazil, eastern Sahara, and southern Australia, while its significant increases appear in the east Pacific, Greenland Sea, Norwegian Sea and Southern Ocean (Fig. 6). In JJA, surface sensible heat flux in the non-uniform CO_2 simulation increases by 0.62 ± 0.34 W m^{-2} and 0.28 ± 0.11 W m^{-2} in the Arctic and southern midlatitudes, respectively, relative to the uniform CO_2 simulation. In DJF, there is a 1.14 ± 0.38 W m^{-2} reduction and 0.45 ± 0.13 W m^{-2} increase in surface sensible heat flux in the Arctic and northern midlatitudes in the non-uniform CO_2 simulation compared with uniform CO_2 simulation (Figs. 4, 6).

Relative to the uniform CO_2 simulation, global annual mean surface latent heat flux decreases by 0.51 ± 0.11 W m^{-2} in the non-uniform CO_2 simulation during 2071–2100, decreasing by 0.48 ± 0.15 W m^{-2} and 0.52 ± 0.12 W m^{-2} over land and over ocean, respectively (Fig. 2g; Table 1). In JJA, there are 0.31 ± 0.28 W m^{-2} and 0.57 ± 0.15 W m^{-2} decreases in surface latent heat flux averaged over land and ocean, respectively (Table A.1). In DJF, surface latent heat flux decreases by 0.58 ± 0.16 W m^{-2} and 0.74 ± 0.23 W m^{-2} over land and over ocean (Table A.2). The reduction in surface latent heat flux is consistent with the global warming in the non-uniform CO_2 simulation (Fig. 2g; Tables 1, A.1, A.2). Land surface latent heat flux is negative in all months, with the maximum reduction in May of 1.23 W m^{-2} under non-uniform

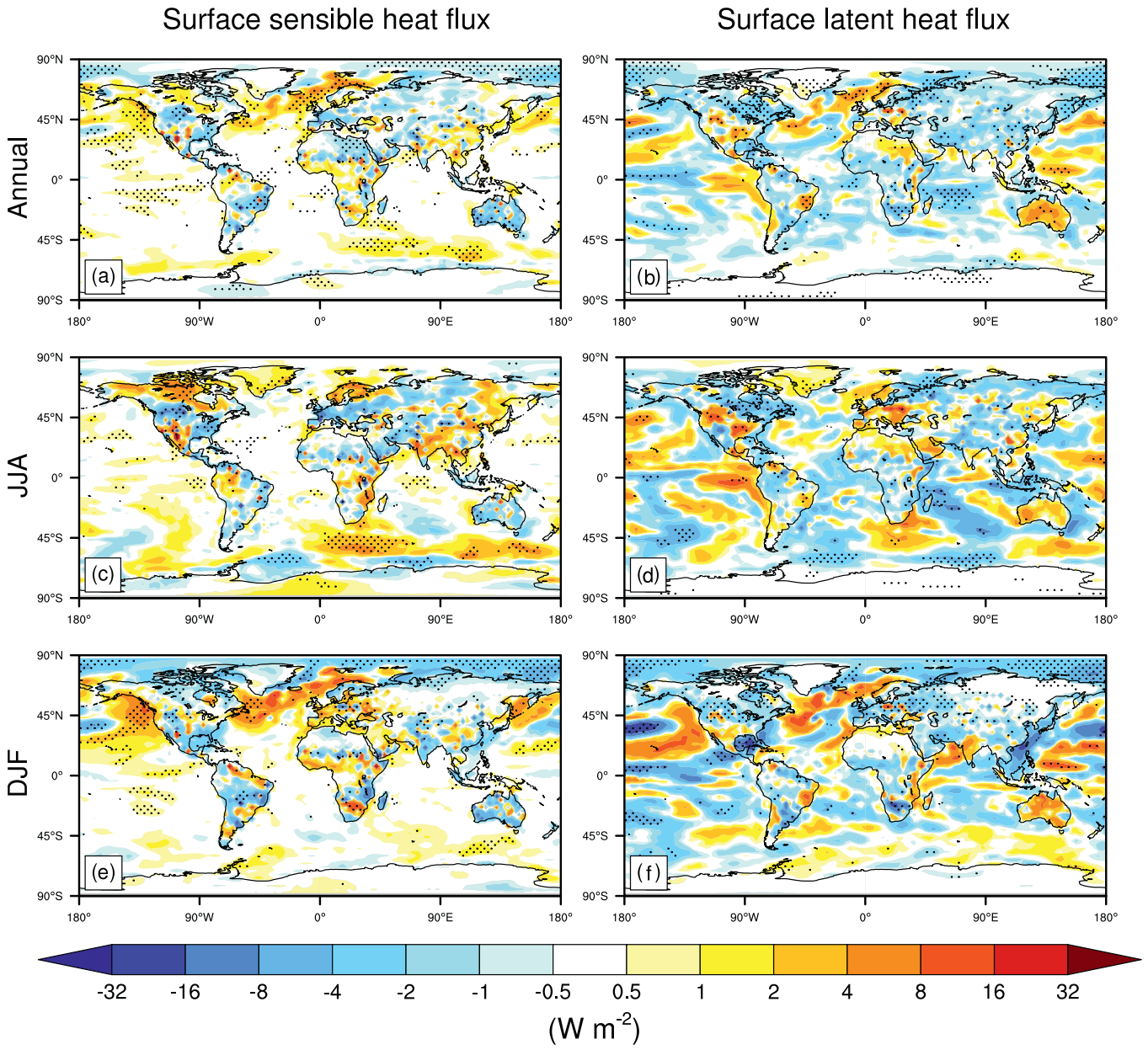

Fig. 6. Maps showing simulated annual mean (a and b), JJA average (c and d), and DJF average (e and f) changes in surface sensible heat flux (W m^{-2}, left column) and surface latent heat flux (W m^{-2}, right column) under non-uniform CO_2 simulation relative to uniform CO_2 simulation during 2071–2100, respectively. Positive values are indicating increases in the downward direction. Stippling areas are regions where changes are statistically significant at the 5% level using the Student's *t*-test.

CO_2 simulation during 2071–2100 (Fig. A.2g). The monthly mean change in surface latent heat flux over ocean fluctuates between 0.1 W $m^{-2}$and − 0.9 W m^{-2} in the non-uniform CO_2 simulation (Fig. A.2g).

Fig. 6 (right column) shows maps of annual mean, JJA average, and DJF average changes in surface latent heat flux under the non-uniform CO_2 simulation relative to uniform CO_2 simulation during 2071–2100. Relative to the uniform CO_2 simulation, there are about 0.5 W m^{-2} decreases in annual mean surface latent heat flux in the northern mid-latitudes, tropics and southern midlatitudes in the non-uniform CO_2 simulation (Figs. 4, 6). In the Arctic, latent heat flux decreases by 0.83 ± 0.16 W m^{-2}. Statistically significant decreases in annual mean surface latent heat flux are primarily located in some areas of the Arctic Ocean, northern Canada, northeast Russia, eastern Indian Ocean, and southern Africa, while significant increases appear in some areas of the southern Greenland, Greenland Sea, Norwegian Sea, eastern Pacific, and central Australia (Fig. 6). In JJA, surface latent heat flux in the non-uniform CO_2 simulation decreases by 0.61 ± 0.25 W m^{-2}, 0.48 ± 0.29 W m^{-2} and 0.76 ± 0.21 W m^{-2} in the Arctic, tropics and southern midlatitudes, respectively, relative to the uniform CO_2 simulation. Statistically significant decreases in JJA mean surface latent heat flux are primarily located in some areas of northern Canada, northeast Russia, and Southern Ocean, while significant increases appear in some areas of southern Greenland (Fig. 6). In DJF, there are about 1.69 ± 0.36 W m^{-2} and 0.95 ± 0.36 W m^{-2} reductions in surface latent heat flux in the Arctic and northern midlatitudes in the non-uniform CO_2 simulation compared with uniform CO_2 simulation (Figs. 4, 6). Statistically significant decreases in DJF mean surface latent heat flux are primarily located in some areas of the Arctic Ocean, Canada, and northeast Russia, Central America, and North Pacific Ocean (Fig. 6).

In the non-uniform CO_2 simulation, the largest changes in Bowen ratio occur at high latitudes, however, these changes are mainly insignificant, and both positive and negative changes occur reflecting the ratio's variability. There are significant increases in the Bowen ratio in Australia, eastern Sahara, northwestern United States, and eastern Brazil

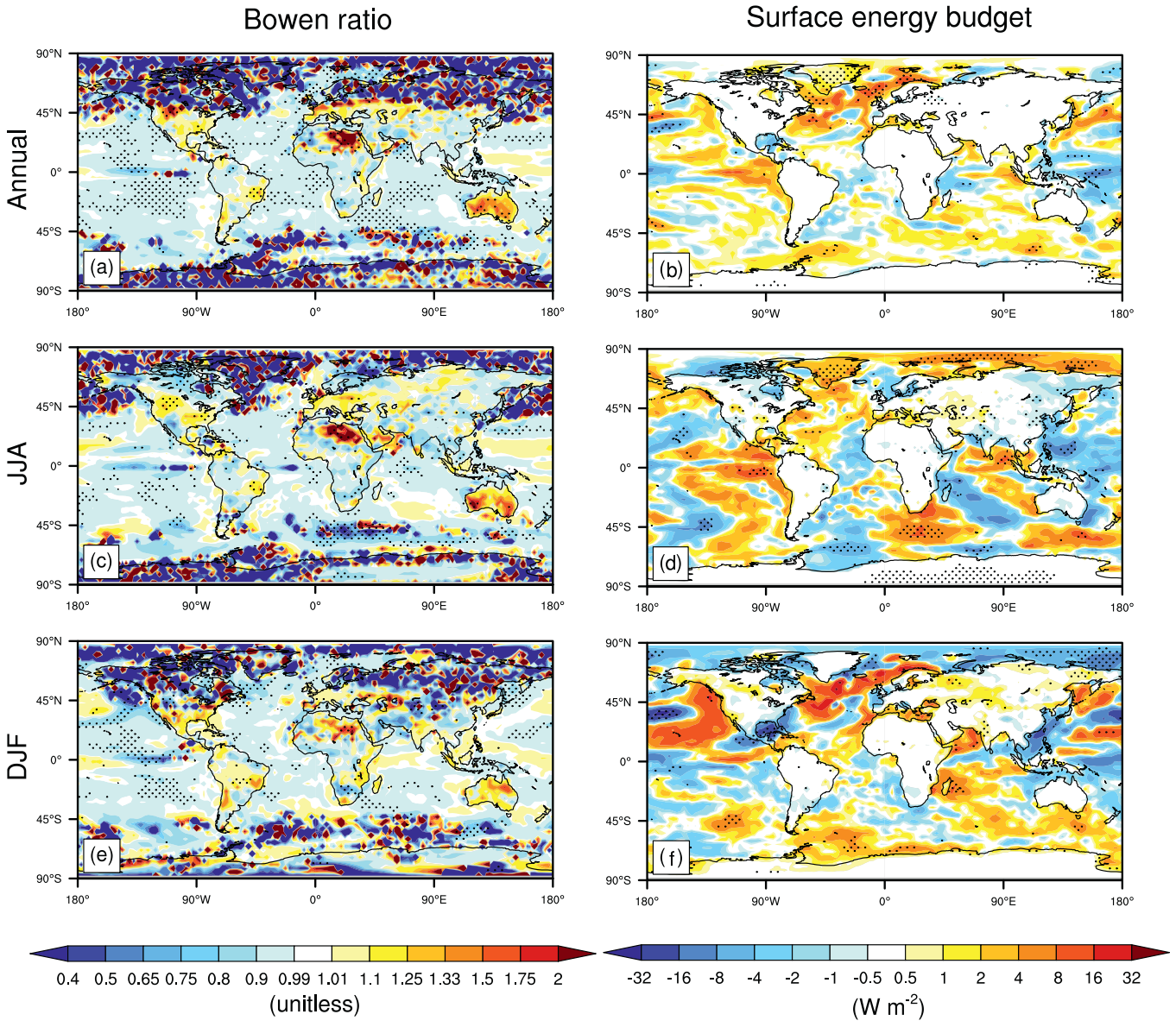

Fig. 7. Maps showing simulated annual mean (a and b), JJA average (c and d), and DJF average (e and f) changes in bowen ratio (¯left column) and surface energy budget (W m^{-2}, right column) under non-uniform CO_2 simulation relative to uniform CO_2 simulation during 2071–2100, respectively. Surface energy budget is sum of shortwave radiative fluxes, longwave radiative fluxes, sensible heat fluxes, and latent heat fluxes (the right side of Eq. (1)). Positive values are indicating increases in the downward direction. Stippling areas are regions where changes are statistically significant at the 5% level using the Student's *t*-test.

compared with the uniform CO_2 simulation (Figs. 6, 7). In some ocean areas, the Bowen ratio is significantly reduced, e.g., eastern Pacific, western Indian Ocean, Greenland Sea, and Southern Ocean in the non-uniform CO_2 simulation. The Bowen ratio decrease in the eastern Pacific is due to changes in both sensible and latent heat fluxes, and the decrease over western Indian Ocean is mainly from the reduction in surface latent heat flux. Over the Greenland Sea and Southern Ocean, the Bowen ratio reduction is determined by increase in surface sensible heat flux.

3.5. Surface energy balance

The bars in Fig. 4 labeled "Budget" are plots of the sum of changes in shortwave radiative fluxes, longwave radiative fluxes, sensible heat fluxes, and latent heat fluxes (the right side of Eq. (1)).This quantity determines how well the surface and atmospheric energy budgets are in balance; when this quantity is nonzero, the surface heat content changes (Boer, 1993).

Relative to the uniform CO_2 simulation, non-uniform CO_2 simulation shows increases in surface energy balance to be 0.25 ± 0.08 W m^{-2} (7.5%) averaged globally, 0.05 ± 0.04 W m^{-2} (9.6%) averaged over land, and 0.33 ± 0.11 W m^{-2} (7.4%) averaged over Ocean during 2071–2100 (Fig. 2h). This indicates heat uptake over this period of the non-uniform CO_2 simulation, which mainly occurs over the ocean. But changes in global mean surface energy budget are not statistically significant in both JJA and DJF (Tables A.1, A.2).

Fig. 7 (right column) shows maps of annual mean, JJA average, and DJF average changes in surface energy budget under non-uniform CO_2 simulation relative to uniform CO_2 simulation during 2071–2100. Relative to the uniform CO_2 simulation, there are increases in annual mean surface energy budget with 0.55 ± 0.38 W m^{-2}, 0.54 ± 0.12 W m^{-2} and 0.40 ± 0.12 W m^{-2} in the Arctic, northern midlatitudes and southern midlatitudes in the non-uniform CO_2 simulation, respectively (Fig. 4). Statistically significant increases in annual mean surface energy budget are primarily located in Greenland, some areas of the Greenland Sea, Norwegian Sea and North Atlantic, while significant decreases appear in some areas of the western Pacific (Fig. 7). In JJA, surface energy budget averaged over the Arctic increases by 0.91 ± 0.68 W m^{-2} in the non-uniform CO_2 simulation, indicating surface heat absorption. Statistically significant increases in JJA mean surface energy budget are primarily located in Greenland, and some areas of the Arctic Ocean, Southern Ocean and East Pacific. while significant decreases appear in some areas of the eastern Pacific (Fig. 7). In DJF, surface energy budget averaged over the Arctic decreases by 1.77 ± 1.00 W m^{-2}. In the northern midlatitudes, southern midlatitudes and Antarctic, increases in surface energy budget are 0.46 ± 0.37 W m^{-2}, 0.48 ± 0.25 W m^{-2} and 0.71 ± 0.25 W m^{-2}, respectively. Statistically significant decreases in DJF mean surface energy budget are primarily located in some areas of the Arctic Ocean (Fig. 7).

4. Summary and discussion

In this study, we assess changes in the surface energy budget considering non-uniform CO_2 distribution using fully coupled BNU-ESM under the business-as-usual RCP8.5 pathway. These changes can be used to understand how the atmosphere adjusts to the non-uniform CO_2 distribution, and in turn how temperature adjusts to these energy flux changes. Global annual mean atmospheric CO_2 concentrations are the same in both the uniform and non-uniform CO_2 simulations. But annual mean CO_2 concentrations increase by 4.11 ± 0.68 ppm over land in the non-uniform CO_2 simulation, and decrease by 1.73 ± 0.68 ppm over ocean. Increases in CO_2 concentrations are up to 18.54 ± 0.72 ppm and 17.92 ± 0.72 ppm in the northern midlatitudes and the Arctic, respectively, during DJF in the non-uniform CO_2 simulation, which is consistent with features of the current observed distribution of CO_2 concentrations (Cao et al., 2019). Relative to the uniform CO_2 simulation, global annual mean of surface air temperature increases by 0.44 ± 0.03 °C when considering non-uniform CO_2 distribution. In the Arctic and the northern midlatitudes, warming is about 1.63 ± 0.28 °C and 0.67 ± 0.08 °C, respectively, during DJF in the non-uniform CO_2 simulation.

The non-uniform CO_2 distribution under RCP8.5 produces a 0.68 ± 0.06 W m^{-2} increase in global annual mean total radiative flux at surface which is mainly produced by increased net downward longwave absorption. Increased global mean downward surface longwave radiative flux (0.73 ± 0.08 W m^{-2}) is primarily due to change in regional CO_2 concentrations, which is slightly offset by associated 0.06 ± 0.03 W m^{-2} reduction in longwave cloud effects. There is a 0.53 ± 0.16 W m^{-2} increase in net downward surface shortwave radiative flux over land in the non-uniform CO_2 simulation, but it decreases by 0.30 ± 0.08 W m^{-2} over ocean that is primarily due to effect of shortwave cloud forcing in some areas of the Arctic Ocean, western Pacific, and Southern Ocean. The non-uniform CO_2 simulation shows a decrease in land sensible heat flux (more net heat flux from the surface to the atmosphere) and an increase in ocean sensible heat flux (reduced net heat flux from the surface to the atmosphere), relative to the uniform CO_2 simulation. Increase in surface sensible heat flux leads to Bowen ratio reduction over the Greenland Sea and Southern Ocean, but there is rather low signal to noise ratio at high latitudes. There is a decrease in global mean latent heat flux (increased net heat flux from the surface to the atmosphere), with a 0.5 W m^{-2} reduction in the northern midlatitudes, tropics and southern midlatitudes in the non-uniform CO_2 simulation. Annual latent heat flux decreases by 0.83 ± 0.16 W m^{-2} in the Arctic, suggesting non-uniform CO_2 induces bigger increases in evaporation than the uniform CO_2 simulation. The non-uniform CO_2 simulation shows an increase in surface energy balance of 0.33 ± 0.11 W m^{-2} (7.4%) averaged over Ocean implying a significant increase in ocean heat uptake. Since most ocean area in in the SH, increased ocean heat uptake is consistent with the northward ocean heat transport, especially in the SH summer (Fig. A.7). In JJA, surface energy budget averaged over the Arctic increases by 0.91 ± 0.68 W m^{-2} in the non-uniform CO_2 simulation, which would be associated with sea ice and feedbacks.

Fig. 8 shows the scattergram of regional changes in atmospheric CO_2 concentration, and surface air temperature, surface total radiative flux, surface energy budgets during 2071–2100 in the non-uniform CO_2 simulation compared with the uniform simulation. Each point is the average of each region during 2071–2100. As may be expected, the slope of regression is very low - about 0.02 °C per ppm of CO_2 for annual mean temperature, 0.03 W m^{-2} per ppm of CO_2 for surface total radiative flux, and 0.02 W m^{-2} per ppm of CO_2 for surface energy budget. The negative regression slope in JJA plots shows the NH high latitude warming or increases in radiative flux dominates over the tropics (Fig. 8d, e, f). All R^2 are less than 0.49, showing that non-regional processes such as atmospheric advection, ocean transport, nonlocal feedback processes are perhaps as important as local changes in radiative forcing. The differences in sensitivity between the regions also illustrates that particular feedbacks and transports vary between regions.

The Arctic clearly is the most sensitive region, perhaps most surprisingly in winter rather than summer. Relative to the uniform CO_2 simulation, there is 0.69 ± 0.15 °C Arctic warming in the JJA, and warming is about 1.63 ± 0.28 °C in DJF. The Arctic winter warming does exceed, and is simulated to far exceed, that in summer where the melting of ice thermostats temperature rises, while the winter warming is unconstrained and is consistent with NH atmospheric energy transport form the tropics (Fig. A.7). The general surface warming in the Arctic is due to local forcing from the spatial difference of CO_2 concentrations and associated feedbacks (Ramanathan et al., 1979; Stuecker et al., 2018). The Arctic shows an increase in net shortwave radiative flux in the non-uniform CO_2. Kravitz et al. (2013b) found a similar pattern under a quadrupled CO_2 simulation and note that it one of the few large-scale robust features of the shortwave feedback response of global warming, and consistent with reduction of sea ice extent (Kravitz et al.,

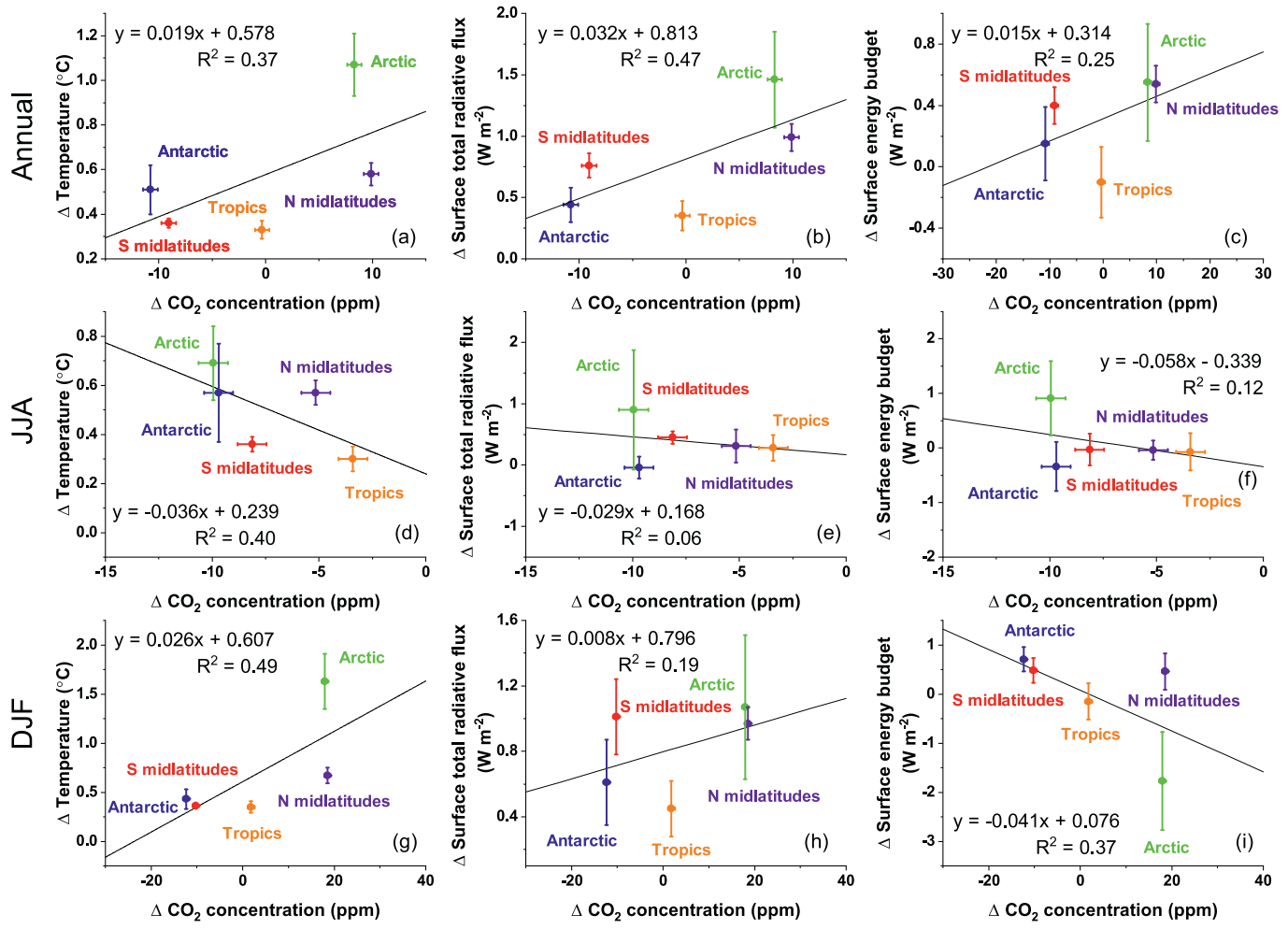

Fig. 8. Scatter plots of annual mean (top row), JJA average (middle row), and DJF average (bottom) between changes in atmospheric CO_2 concentration (ppm), and changes in surface air temperature (°C, left column), changes in surface total radiative flux (W m^{-2}, middle column), changes in surface energy budget (W m^{-2}, middle column), respectively, in the non-uniform CO_2 simulation compared with the uniform CO_2 simulation during 2071–2100. The plotted colored points represent the mean of all grid points in each region and the error bars are standard error.

2013a). Statistically significant increases in JJA mean surface energy budget are primarily located in Greenland, and some areas of the Arctic Ocean, indicating surface heat absorption, which would be associated with ice melting and its feedbacks. The Arctic warming is partially offset by the cloud effect, especially during summer season (see Section 3.3), in the non-uniform CO_2 simulation.

Climate modeling taking into account the CO_2 distribution goes some way toward addressing some of the known biases in temperature in the historical simulations (Navarro et al., 2018). This suggests that including the heterogenous CO_2 distribution could enhance the realism of global climate modeling. Using BNU-ESM, global mean surface air temperature is in the inhomogeneous CO_2 simulations is approximately 0.3 °C lower than in the spatially uniform runs over the historical period from 1986 to 2005, reducing the warming bias seen in the uniform runs compared with the HadCRUT4 observations (Wang et al., 2020). In CESM, spatially homogeneous CO_2 simulations overestimated climate warming over the Arctic and tropical Pacific, while underestimating warming in the mid-latitudes over most land areas (Zhang et al., 2019). The inhomogeneous 1950–2000 runs simulated by CESM produce lower temperatures at both poles than the homogeneous runs, by up to 1.5 °C including statistically significant cooling over the Barents Sea area (Navarro et al., 2018).

In the historical period, direct radiative forcing from inhomogeneous CO_2 variations of around 10 ppm only leads to radiative forcing differences of 0.1–0.2 W m^{-2} (Wang et al., 2020). In addition to direct radiative effects, surface air temperature responds to non-local advection through changes in large scale atmospheric circulations (Cheng et al., 2022a; Zhang et al., 2019). Underestimated climate warming over the Artic and the tropical Pacific and overestimated warming at mid-latitudes are seen in the homogeneous CO_2 historical simulations (Wang et al., 2020; Zhang et al., 2019). In spatially inhomogeneous CO_2 simulations these biases are reduced via an intensified meridional heat exchange between mid- and high latitudes in the northern hemisphere and a weakened westerly jet due to lower radiative forcing over western Eurasia (Wang et al., 2020; Zhang et al., 2019). Non-uniform CO_2 based on the AIRS mid-tropospheric distribution induced variability with similar wavelengths, velocity and spatial patterns as Rossby waves (Ying et al., 2020). Our analysis of non-uniform CO_2 distribution under RCP8.5 shows a decrease in annual mean total (atmosphere plus ocean) heat transport in the NH low and mid latitudes (Equator - 60°N), with no change in high latitude (Fig. A.7). These transport anomalies are a few percent of the typical meridional heat transport values (Wunsch, 2005). This suggests the total heat transport does not contribute to the warming in the NH under non-uniform CO_2, though there is an increase in NH winter atmospheric heat transport from the tropics to the Arctic.

Local surface air temperature anomalies under nonuniform CO_2 simulations are also affected by the CO_2 physiological response over vegetated areas. Land plants adjust to changes in atmospheric CO_2 by altering their stomatal conductance, which consequently affects the water evapotranspiration from plant leaf to atmosphere (Skinner et al.,

2018). This affects environmental temperature through evaporative cooling, and the evaporated moisture alters the air humidity and influences low cloud amounts via water vapor advection, which is especially obvious in summer when the plants grow vigorously. Under non-uniform CO_2 in RCP8.5, there are increases in JJA mean surface latent heat flux (positive values are indicating increases in the downward direction; an energetic perspective on evapotranspiration (ET)) in the eastern United States, South America, western Europe, India, and eastern China (Fig. 6). The decreases in ET here are consistent with local increases in CO_2 and the plant physiological effect. In the polar areas, the degree of warming amplification depends strongly on the locally factors (Stuecker et al., 2018), specifically elevated CO_2 concentrations in the Arctic, through positive local lapse-rate feedback, with ice-albedo and Planck feedbacks playing subsidiary roles. Under non-uniform CO_2 RCP8.5, the Arctic surface energy budget increases by 0.91 ± 0.68 W m^{-2} in JJA (Fig. 7), a significant increase in Arctic heat uptake, which would have an impact on the Greenland ice sheet (such as a larger summer melt region) and sea ice extent. In marine ecosystems, non-uniform atmospheric CO_2 and temperature biases could affect the uptake and storage of CO_2 in the ocean, which will affect regional atmospheric CO_2 concentrations, ocean pH, ocean oxygen concentrations and primary production (Nagelkerken and Connell, 2015).

There are few studies with global or regional climate models simulating the effects of inhomogeneous atmospheric CO_2 distribution. Almost all current studies using CO_2 distributions are taken form national-level monthly or annual CO_2 emissions weighted by the grid's population density, or from daily satellite retrievals. The temporal resolution of distributed CO_2 data should be increased to diurnal to reduce the biases from physiological forcing effects. We have shown with only with an energetic perspective the significant impacts that non-uniform CO2 distribution has on surface temperatures and hence global energy and moisture transport pathways. Improved understanding of the earth system response would require a handful of common standard experiments undertaken by a variety of climate models, at least ranging from earth System Models to regional climate models. The complexity of the response implies sophisticated coupled models should be used for intercomparison. The overall impact on global mean temperatures of inhomogeneous CO_2 forcing leads to a significant reduction in estimated remaining carbon emissions available to meet politically agreed climate targets. While this is should in no way be construed as casting doubt on the imperative of rapid emissions reductions, it may lead to better assessment of regional impacts from climate warming.

Data availability

Data from the simulations used in this work is available at https://simlab.quickconnect.cn/d/s/m5reKsJfzw3O7ayldIpalGd21s5oSWER/TZ9kjLhdglbfP63qGYZ3vWpi4vimz6Wv-07gAYV0ICQk, and non-uniform CO_2 file can be accessed by https://doi.org/10.5281/zenodo.5021361.

CRediT authorship contribution statement

Wei Cheng: Conceptualization, Formal analysis, Writing – original draft. **Xiaonan Duan:** Methodology, Writing – review & editing, Validation. **John C. Moore:** Conceptualization, Writing – review & editing, Validation. **Xiangzheng Deng:** Conceptualization, Writing – review & editing, Investigation. **Yong Luo:** Methodology, Writing – review & editing, Investigation. **Lei Huang:** Methodology, Writing – review & editing, Validation. **Yongli Wang:** Data curation, Writing – review & editing, Validation.

Declaration of Competing Interest

The authors declared that they have no conflicts of interest to this work.

Acknowledgements

This research was supported by the National Key Research and Development Program of China (Grant No. 2016YFA0602500; Grant No. 2017YFA0603703) and the Strategic Priority Research Program of Chinese Academy of Sciences (Grant No. XDA23070400). Wei Cheng was supported by the research start-up project for new recruits at Institute of Geographic Sciences and Natural Resources Research, Chinese Academy of Sciences. The authors would like to thank Li Dan and Jinming Feng for the manuscript revision and help in conducting simulation experiments.

Appendix A. Supplementary data

Supplementary information to this article can be found online at https://doi.org/10.1016/j.atmosres.2022.106196.

References

Andrews, T., Forster, P., Gregory, J., 2009. A surface energy perspective on climate change. J. Clim. 22, 2557–2570. https://doi.org/10.1175/2008JCLI2759.1.

Ban-Weiss, G., Bala, G., Cao, L., Pongratz, J., Caldeira, K., 2011. Climate forcing and response to idealized changes in surface latent and sensible heat. Environ. Res. Lett. 6, 034032 https://doi.org/10.1088/1748-9326/6/3/034032.

Boer, G., 1993. Climate change and the regulation of the surface moisture and energy budgets. Clim. Dyn. 8, 225–239. https://doi.org/10.1007/BF00198617.

Bracegirdle, T., Shuckburgh, E., Sallee, J., Wang, Z., Meijers, A., Bruneau, N., Phillips, T., Wilcox, L., 2013. Assessment of surface winds over the Atlantic, Indian, and Pacific Ocean sectors of the Southern Ocean in CMIP5 models: historical bias, forcing response, and state dependence. J. Geophys. Res.-Atmos. 118, 547–562. https://doi.org/10.1002/jgrd.50153.

Cao, L., Chen, X., Zhang, C., Kurban, A., Qian, J., Pan, T., Yin, Z., Qin, X., Ochege, F., Maeyer, P., 2019. The global spatiotemporal distribution of the mid-tropospheric CO_2 concentration and analysis of the controlling factors. Remote Sens. 11, 94. https://doi.org/10.3390/rs11010094.

Chahine, M., Barnet, C., Olsen, E., Chen, L., Maddy, E., 2005. On the determination of atmospheric minor gases by the method of vanishing partial derivatives with application to CO_2. Geophys. Res. Lett. 32, L22803. https://doi.org/10.1029/2005GL024165.

Chahine, M., Chen, L., Dimotakis, P., Jiang, X., Li, Q., Olsen, E., Pagano, T., Randerson, J., Yung, Y., 2008. Satellite remote sounding of mid-tropospheric CO_2. Geophys. Res. Lett. 35, L17807. https://doi.org/10.1029/2008GL035022.

Chen, L., Yu, Y., Sun, D., 2013. Cloud and water vapor feedbacks to the El Niño warming: are they still biased in CMIP5 models? J. Clim. 26, 4947–4961. https://doi.org/10.1175/JCLI-D-12-00575.1.

Cheng, W., Dan, L., Deng, X., Feng, J., Wang, Y., Peng, J., Tian, J., Qi, W., Liu, Z., Zheng, X., Zhou, D., Jiang, S., Zhao, H., Wang, X., 2022b. Global monthly gridded atmospheric carbon dioxide concentrations under the historical and future scenarios. Sci. Data 9, 83. https://doi.org/10.1038/s41597-022-01196-7.

Cheng, W., MacMartin, D., Kravitz, B., Visioni, D., Bednarz, E., Xu, Y., Luo, Y., Huang, L., Hu, Y., Staten, P., Hitchcock, P., Moore, J., Guo, A., Deng, X., 2022a. Changes in Hadley circulation and intertropical convergence zone under strategic stratospheric aerosol geoengineering. npj Clim. Atmos. Sci. 5, 32 https://doi.org/10.1038/s41612-022-00254-6.

Cheng, W., Moore, J., Cao, L., Ji, D., Zhao, L., 2017. Simulated climate effects of desert irrigation geoengineering. Sci. Rep. 7, 46443. https://doi.org/10.1038/srep46443.

Cheng, W., Dan, L., Deng, X., Feng, J., Wang, Y., Peng, J., Tian, J., Qi, W., Liu, Z., Zheng, X., Zhou, D., Jiang, S., Zhao, H., Wang, X., 2021. Global Monthly Distributions of Atmospheric CO_2 Concentrations under the Historical and Future Scenarios. doi:10.5281/zenodo.5021361.

Dai, Y., Zeng, X., Dickinson, R., Baker, I., Bonan, G., Bosilovich, M., Denning, A., Dirmeyer, P., Houser, P., Niu, G., Oleson, K., Schlosser, C., Yang, Z., 2003. The common land model. Bull. Amer. Meteor. Soc. 84, 1013–1024. https://doi.org/10.1175/BAMS-84-8-1013.

Erickson III, D., Mills, R., Gregg, J., Blasing, T., Hoffman, F., Andres, R., Devries, M., Zhu, Z., Kawa, S., 2008. An estimate of monthly global emissions of anthropogenic CO_2: Impact on the seasonal cycle of atmospheric CO_2. J. Geophys. Res.-Biogeosci. 113, G01023. https://doi.org/10.1029/2007JG000435.

Griffies, S.M., 2010. Elements of MOM4p1, GFDL Ocean Group Technical Report No. 6.

Gu, L., Meyers, T., Pallardy, S., Hanson, P., Yang, B., Heuer, M., Hosman, K., Riggs, J., Sluss, D., Wullschleger, S., 2006. Direct and indirect effects of atmospheric conditions and soil moisture on surface energy partitioning revealed by a prolonged drought at a temperate forest site. J. Geophys. Res.-Atmos. 111, D16102. https://doi.org/10.1029/2006JD007161.

Hunke, E., Lipscomb, W., 2010. CICE: The Los Alamos Sea Ice Model user's Manual, version 4.1. Los Alamos National Laboratory.

Ji, D., Wang, L., Feng, J., Wu, Q., Cheng, H., Zhang, Q., Yang, J., Dong, W., Dai, Y., Gong, D., Zhang, R.-H., Wang, X., Liu, J., Moore, J.C., Chen, D., Zhou, M., 2014. Description and basic evaluation of Beijing Normal University Earth System Model

(BNU-ESM) version 1. Geosci. Model Dev. 7, 2039–2064. https://doi.org/10.5194/gmd-7-2039-2014.

Kravitz, B., Caldeira, K., Boucher, O., Robock, A., Rasch, P.J., Alterskjær, K., Karam, D.B., Cole, J.N.S., Curry, C.L., Haywood, J.M., Irvine, P.J., Ji, D., Jones, A., Kristjánsson, J. E., Lunt, D.J., Moore, J.C., Niemeier, U., Schmidt, H., Schulz, M., Singh, B., Tilmes, S., Watanabe, S., Yang, S., Yoon, J.-H., 2013a. Climate model response from the Geoengineering Model Intercomparison Project (GeoMIP). J. Geophys. Res.-Atmos. 118, 8320–8332. https://doi.org/10.1002/jgrd.50646.

Kravitz, B., Rasch, P.J., Forster, P.M., Andrews, T., Cole, J.N.S., Irvine, P.J., Ji, D., Kristjánsson, J.E., Moore, J.C., Muri, H., Niemeier, U., Robock, A., Singh, B., Tilmes, S., Watanabe, S., Yoon, J.-H., 2013b. An energetic perspective on hydrological cycle changes in the Geoengineering Model Intercomparison Project. J. Geophys. Res.-Atmos. 118, 13,087–13,102. https://doi.org/10.1002/2013JD020502.

Kuang, Z., Margolis, J., Toon, G., Crisp, D., Yung, Y., 2002. Spaceborne measurements of atmospheric CO_2 by high-resolution NIR spectrometry of reflected sunlight: an introductory study. Geophys. Res. Lett. 29, 11-1–11-4. https://doi.org/10.1029/2001GL014298.

Kuze, A., Suto, H., Nakajima, M., Hamazaki, T., 2009. Thermal and near infrared sensor for carbon observation Fourier-transform spectrometer on the Greenhouse gases observing Satellite for greenhouse gases monitoring. Appl. Optics 48, 6716–6733. https://doi.org/10.1364/AO.48.006716.

Lengler, U., De Lucia, M., Kühn, M., 2010. The impact of heterogeneity on the distribution of CO_2: Numerical simulation of CO_2 storage at Ketzin. Int. J. Greenh. Gas Control 4, 1016–1025. https://doi.org/10.1016/j.ijggc.2010.07.004.

Meinshausen, M., Smith, S., Calvin, K., Daniel, J., Kainuma, M., Lamarque, J., Matsumoto, K., Montzka, S., Raper, S., Riahi, K., Thomson, A., Velders, G., van Vuuren, D., 2011. The RCP greenhouse gas concentrations and their extensions from 1765 to 2300. Clim. Change 109, 213–241. https://doi.org/10.1007/s10584-011-0156-z.

Nagelkerken, I., Connell, S., 2015. Global alteration of ocean ecosystem functioning due to increasing human CO_2 emissions. Proc. Natl. Acad. Sci. U. S. A. 112, 13272–13277. https://doi.org/10.1073/pnas.1510856112.

Navarro, A., Moreno, R., Tapiador, F., 2018. Improving the representation of anthropogenic CO_2 emissions in climate models: impact of a new parameterization for the Community Earth System Model (CESM). Earth Syst. Dynam. 9, 1045–1062. https://doi.org/10.5194/esd-9-1045-2018.

Neale, R., Richter, J., Park, S., Lauritzen, P., Vavrus, S., Rasch, P., Zhang, M., 2013. The mean climate of the community atmosphere model (CAM4) in Forced SST and fully coupled experiments. J. Clim. 26, 5150–5168. https://doi.org/10.1175/JCLI-D-12-00236.1.

Ramanathan, V., Lian, M., Cess, R., 1979. Increased atmospheric CO_2: Zonal and seasonal estimates of the effect on the radiation energy balance and surface temperature. J. Geophys. Res.-Oceans 84, 4949–4958. https://doi.org/10.1029/JC084iC08p04949.

Sanderson, B., 2020. Relating climate sensitivity indices to projection uncertainty. Earth Syst. Dynam. 11, 721–735. https://doi.org/10.5194/esd-11-721-2020.

Schimel, D., Melillo, J., Tian, H., McGuire, A., Kicklighter, D., Kittel, T., Rosenbloom, N., Running, S., Thornton, P., Ojima, D., Parton, W., Kelly, R., Sykes, M., Neilson, R., Rizzo, B., 2000. Contribution of increasing CO_2 and climate to carbon storage by ecosystems in the United States. Science 287, 2004–2006. https://doi.org/10.1126/science.287.5460.2004.

Skinner, C., Poulsen, C., Mankin, J., 2018. Amplification of heat extremes by plant CO_2 physiological forcing. Nat. Commun. 9, 1094. https://doi.org/10.1038/s41467-018-03472-w.

Stuecker, M., Bitz, C., Armour, K., Proistosescu, C., Kang, S., Xie, S., Kim, D., McGregor, S., Zhang, W., Zhao, S., Cai, W., Dong, Y., Jin, F., 2018. Polar amplification dominated by local forcing and feedbacks. Nat. Clim. Chang. 8, 1076–1081. https://doi.org/10.1038/s41558-018-0339-y.

Tian, D., Dong, W., Yan, X., Chou, J., Yang, S., Wei, T., Zhang, H., Guo, Y., Wen, X., Yang, Z., 2016. Climate system responses to a common emission budget of carbon dioxide. J. Clim. 29, 2433–2442. https://doi.org/10.1175/JCLI-D-15-0213.1.

Wang, T., Shi, J., Jing, Y., Xie, Y., 2013. Investigation of the consistency of atmospheric CO_2 retrievals from different space-based sensors: Intercomparison and spatiotemporal analysis. Chin. Sci. Bull. 58, 4161–4170. https://doi.org/10.1007/s11434-013-5996-7.

Wang, Y., Feng, J., Dan, L., Lin, S., Tian, J., 2020. The impact of uniform and nonuniform CO_2 concentrations on global climatic change. Theor. Appl. Climatol. 139, 45–55. https://doi.org/10.1007/s00704-019-02924-7.

Wei, T., Yang, S., Moore, J., Shi, P., Cui, X., Duan, Q., Xu, B., Dai, Y., Yuan, W., Wei, X., Yang, Z., Wen, T., Teng, F., Gao, Y., Chou, J., Yan, X., Wei, Z., Guo, Y., Jiang, Y., Gao, X., Wang, K., Zheng, X., Ren, F., Lv, S., Yu, Y., Liu, B., Luo, Y., Li, W., Ji, D., Feng, J., Wu, Q., Cheng, H., He, J., Fu, C., Ye, D., Xu, G., Dong, W., 2012. Developed and developing world responsibilities for historical climate change and CO_2 mitigation. Proc. Natl. Acad. Sci. U. S. A. 109, 12911–12915. https://doi.org/10.1073/pnas.1203282109.

Wunch, D., Wennberg, P., Toon, G., Connor, B., Fisher, B., Osterman, G., Frankenberg, C., Mandrake, L., O'Dell, C., Ahonen, P., Biraud, S., Castano, R., Cressie, N., Crisp, D., Deutscher, N., Eldering, A., Fisher, M., Griffith, D., Gunson, M., Heikkinen, P., Keppel-Aleks, G., Kyrö, E., Lindenmaier, R., Macatangay, R., Mendonca, J., Messerschmidt, J., Miller, C., Morino, I., Notholt, J., Oyafuso, F., Rettinger, M., Robinson, J., Roehl, C., Salawitch, R., Sherlock, V., Strong, K., Sussmann, R., Tanaka, T., Thompson, D., Uchino, O., Warneke, T., Wofsy, S., 2011. A method for evaluating bias in global measurements of CO_2 total columns from space. Atmos. Chem. Phys. 11, 12317–12337. https://doi.org/10.5194/acp-11-12317-2011.

Wunsch, C., 2005. The total meridional heat flux and its oceanic and atmospheric partition. J. Clim. 18, 4374–4380. https://doi.org/10.1175/JCLI3539.1.

Xie, X., Huang, X., Wang, T., Li, M., Li, S., Chen, P., 2018. Simulation of Non-Homogeneous CO_2 and its impact on regional temperature in East Asia. J. Meteorol. Res. 32, 456–468. https://doi.org/10.1007/s13351-018-7159-x.

Yang, D., Liu, Y., Feng, L., Wang, J., Yao, L., Cai, Z., Zhu, S., Lu, N., Lyu, D., 2021. The first global carbon dioxide flux map derived from TanSat measurements. Adv. Atmos. Sci. 38 (9), 1433–1443. https://doi.org/10.1007/s00376-021-1179-7.

Ying, N., Zhou, D., Han, Z.G., Chen, Q.H., Ye, Q., Xue, Z.G., 2020. Rossby waves detection in the CO_2 and temperature multilayer climate network. Geophys. Res. Lett. 47, e2019GL086507 https://doi.org/10.1029/2019GL086507.

Zhang, X., Li, X., Chen, D., Cui, H., Ge, Q., 2019. Overestimated climate warming and climate variability due to spatially homogeneous CO_2 in climate modeling over the Northern Hemisphere since the mid-19 th century. Sci. Rep. 9, 1–9. https://doi.org/10.1038/s41598-019-53513-7.